




# The role of three-dimensional fault interactions in creating complex seismic sequences

## Journal Article

### Author(s):

Yin, Yifan ; Galvez, Percy; Heimisson, Elías Rafn ; Wiemer, Stefan 

### Publication date:

2023-03-15

### Permanent link:

<https://doi.org/10.3929/ethz-b-000601601>

### Rights / license:

[Creative Commons Attribution-NonCommercial 4.0 International](#)

### Originally published in:

Earth and Planetary Science Letters 606, <https://doi.org/10.1016/j.epsl.2023.118056>

### Funding acknowledgement:

20-2 FEL-19 - Seismic or Aseismic? Towards Enhanced Geothermal Systems without Large Earthquakes (ETHZ)



# The role of three-dimensional fault interactions in creating complex seismic sequences



Yifan Yin<sup>a,\*</sup>, Percy Galvez<sup>b</sup>, Elías Rafn Heimisson<sup>a</sup>, Stefan Wiemer<sup>a</sup>

<sup>a</sup> Swiss Seismological Service, ETH Zürich, Sonneggstrasse 5, 8009, Zürich, Switzerland

<sup>b</sup> King Abdullah University of Science and Technology, Thuwal, 23955-6900, Kingdom of Saudi Arabia

## ARTICLE INFO

### Article history:

Received 15 September 2022  
 Received in revised form 3 February 2023  
 Accepted 13 February 2023  
 Available online 27 February 2023  
 Editor: R. Bendick

### Keywords:

earthquake interaction  
 strike-slip faults  
 rate-and-state friction  
 fault system  
 recurrence time  
 earthquake cycle

## ABSTRACT

A physics-based earthquake simulator should reproduce first-order empirical power-law behaviors of magnitudes and clustering. These laws have emerged spontaneously in either discrete or low-dimension continuum simulations without power-law or stochastic heterogeneity. We show that the same emergence can occur in 3-D continuum simulations with fault interactions and rate-and-state friction. Our model approximates a strike-slip fault system as three *en echelon* faults. Simulations show spatio-temporally clustered earthquake sequences exhibiting characteristic Gutenberg-Richter scaling as well as empirical inter-event time distribution. The Gutenberg-Richter scaling occurs only in partial ruptures that result from fault interactions. With fault interactions, partial ruptures emerge when seismogenic width  $W$  over characteristic nucleation length  $L_\infty$  is larger than 16.24, but none occur without fault interaction. The mainshock recurrence times of individual faults remain quasi-periodic. The system mainshock recurrence time is a combination of short-term Omori-type decay and Brownian passage time. Higher  $W/L_\infty$  increase short-term clustering probability to at most 30%. These results indicate that physics-based multi-cycle models adequately reflect observed statistical signatures and show practical potential for long-term hazard assessment and medium-term forecasting.

© 2023 The Author(s). Published by Elsevier B.V. This is an open access article under the CC BY-NC license (<http://creativecommons.org/licenses/by-nc/4.0/>).

## 1. Introduction

Empirical seismicity, earthquake rupture, and fault observations are inherently multiscale in space and time (Ben-Zion, 2008). To simulate earthquake sequences, existing models of earthquake processes either adopt a statistical approach to produce stochastic seismic sequences (e.g., Ogata, 1988), or create cellular-automaton models with fault system geometries to generate synthetic seismicity (e.g., Rundle, 1988; Robinson and Benites, 1995; Tullis et al., 2012). On the other hand, numerical studies of the source process use continuum approaches to simulate the details of earthquake cycles on a single fault (e.g., Tse and Rice, 1986; Rice, 1993; Lapusta et al., 2000). While cellular-automaton earthquake simulators successfully aid time-independent seismic hazard assessments (Shaw et al., 2018; Milner et al., 2021), continuum models of sequences of earthquakes and aseismic slip (SEAS) have the potential to forecast time-dependent ruptures as computation power advances (Erickson et al., 2020; Jiang et al., 2022). However, natural seismicity consists of distinct spatiotemporal distributions that do

not necessary exist in SEAS models. In addition, there lacks studies of earthquake interactions within continuum models, a prominent component in cellular automaton models. How do the nucleation and rupture extent, and eventually the mainshock recurrence time of SEAS simulations response to fault interaction? Such insight is vital for enhancing process understanding and improving the long-term time-dependent forecast of probabilistic seismic hazard assessment (PSHA) (Field, 2019).

Earthquake catalogs can be considered as point processes, where earthquakes are discrete in time and follow well-known empirical distributions. The earthquake size distribution follows the Gutenberg-Richter power law (Gutenberg and Richter, 1944), aftershock, and foreshock statistics follow the Omori-Utsu law (Omori, 1895; Utsu, 1961), and inter-event time can be described using the Omori-Utsu law plus Poisson process (Saichev and Sornette, 2007). These empirically observed laws are the foundations of statistical models such as the Epidemic-Type Aftershock Sequence (ETAS) model (Ogata, 1988). ETAS can reproduce and forecast the seismicity surprisingly well, generally outperforming physics-based models in retrospective and prospective experiments, especially for aftershock forecasts (Ogata, 1988; Schorlemmer et al., 2018). Although ETAS-type models are shown to be successful for operational earthquake forecasts for short horizons

\* Corresponding author.

E-mail address: [yifany@protonmail.ch](mailto:yifany@protonmail.ch) (Y. Yin).

(Taroni et al., 2018), a long-term assessment still requires fault-based seismicity evaluated based on observations (e.g., geodesy, historical earthquake catalogs, paleoseismology) combined with first-order physical concepts like elastic rebound as the basis (Field et al., 2017).

Another way to describe discrete complex systems such as seismicity is cellular automaton models. These models use simplified rules of interaction as an analogy to stress transfer and produce power-law statistics similar to natural seismicity (Bak and Tang, 1989; Huang and Turcotte, 1990; Jiménez, 2013). By fitting the model geometry to fault systems, they can produce long synthetic catalogs directly from fault geometry and their slip rates. The RSQSim simulator is particularly successful in that it incorporates a simplified version of rate-and-state friction (RSF) and mitigates the influence of grid dependence on rupture propagation by altering the friction law in an *ad-hoc* manner. The simplified rules of event triggering vastly increase the computational speed for earthquake generation by skipping the interseismic evolution. The approximations allow RSQSim to create sequences that satisfy scaling laws, foreshock, and aftershock clustering (Dieterich and Richards-Dinger, 2010; Richards-Dinger and Dieterich, 2012). It also helps to explore the range of possible ruptures within a given fault system. The rupture history generated can also be aggregated into ground motion hazard curves (Shaw et al., 2018; Milner et al., 2021, 2022).

However, the cellular automaton simulators are still inherently discrete in both time-stepping and in space. The generated earthquake sequences are fully deterministic depending on the specific model setup (Milner et al., 2021), meaning a slight change of mesh would alter the sequence altogether, albeit with similar statistical properties. Omitting interseismic evolution also means not resolving the aseismic slips behaviors like slow-slip events, if not otherwise explicitly tailor the model for them (Colella et al., 2011).

Researchers use cellular-automata models for synthetic seismicity because using a well-resolved continuum model is computationally expensive. Discrete models indeed show agreement with the complexity and statistical laws of real earthquake sequences. The RSQSim simulator is particularly successful in that it incorporates a simplified version of rate-and-state friction (RSF) to create sequences that satisfy scaling laws and foreshock and aftershock clustering (Dieterich and Richards-Dinger, 2010; Richards-Dinger and Dieterich, 2012). However, the simulator is still inherently discrete. This means that if one changes the grid size or meshing method, the resulting earthquake sequences will also change, albeit with similar statistical properties. While given the same initial condition, well-resolved continuum simulations will give very similar sequence regardless of the software and numerical method (Jiang et al., 2022). The RSQSim simulator mitigates the influence of grid dependence on rupture propagation by altering the friction law in an *ad-hoc* manner (Richards-Dinger and Dieterich, 2012).

If we solve the continuum equations of friction and stress instead, the complexity is greatly reduced and frequently a single characteristic event or bimodal ruptures emerges (Rice, 1993; Lapusta et al., 2000). The continuum limit is attained when the smallest physical length scale is several times larger than the spatial discretization of the fault. This critical size is generally considered to be the cohesive zone width of the rupture front during seismic slip (Lapusta et al., 2000; Rubín and Ampuero, 2005; Day et al., 2005). A simulation that satisfies the continuum limit typically does not produce clustered, power-law distributed seismicity, unless this is imposed through heterogeneity. For example, by setting a distribution of critical slip distance on the fault surface (Hillers et al., 2007; Dublanche, 2020). Inherently discrete simulations spontaneously manifest fundamental and ubiquitous statistical properties of earthquakes without such laws being described

or conditioned, while continuum simulations appear to only do so if the right kind of heterogeneity is assumed.

At first glance, it may seem like the discrete simulations intrinsically capture some fundamental physics not captured by the much smoother continuum simulations. However, we have recently started to understand that continuum simulations can also spontaneously manifest such statistical laws even on a uniform 1-D fault in a 2-D space given appropriate frictional parameters and reducing critical slip length (Cattania, 2019; Barbot, 2019; Heimisson, 2020).

In earthquake cycles simulated with rate-and-state friction law, partial ruptures, or events that arrest before propagating the whole fault, begin to emerge on a frictionally uniform fault above a certain length-scale threshold, creating events smaller than the characteristic events. Particularly, the emergence follows the ratio between seismogenic patch width and characteristic nucleation size  $W/L_\infty$  where  $L_\infty$  is controlled by the RSF parameters (See section 2) (Lapusta et al., 2000). Cattania (2019) systematically explored the parameter space using 1-D fault simulations and showed that the partial rupture emerge when increasing the ratio above  $10^1$ . The  $b$  value of frequency-magnitude distribution grows as this ratio grows, with the extreme case of  $b > 3/4$  at  $W/L_\infty = 1000$ .

Recreating such result in 2-D planar fault by increasing the  $W/L_\infty$  ratio means a squared increase in model size and accompanying stress interactions between each patch that updates at every iteration. The vast difference in timescales between interseismic time (tens to hundreds of years) and seismic ruptures (tens to hundreds of seconds) also increase the time stepping difficulty. These two factors restrict the majority of current SEAS models to study the earthquake cycles on a single seismogenic patch, or two with reduced order (e.g., Jiang et al., 2022; Lambert and Lapusta, 2021). Further, robust catalog statistics require sufficient number of events, meaning a long simulated period covering multiple full cycles with smaller earthquakes in between. In this paper, we generate such robust catalogs on 3D fault structures. We seek to explore how fault structure influences earthquake statistics and in a 3D simulated fault system that is a closer analog to segmented crustal fault systems.

To overcome the computation barrier and perform multi-fault simulations, we first improve the numerical efficiency of the quasi-dynamic rupture simulation code appendix A. The improvement allows for a total of eight well resolved simulations consisting of three interacting faults in a 3-D half-space, each producing more than 100 seismic events.

We further find that in fault system simulations, stress heterogeneity created by faults interaction cause rupture arrest, thus creating different earthquake magnitudes at a larger length scale needed for a single fault. We explore an *en echelon* setup, which is one of the simplest fault geometry structures that exist in nature and is well constrained by geological studies (Fig. 1) (de Jossineau and Aydin, 2007, 2009). These partial events and stress disturbances result in complex sequences that follow the empirical inter-event time distribution and clear mainshock clustering. Our parameter exploration produces a range of seismic behavior, from synchronized clusters at smaller  $W/L_\infty$  ratio to clustered full and partial ruptures as  $W/L_\infty$  increases.

The paper first briefly discusses the methodology and model setup in section 2. Then we present results of a single fault and then *en echelon* fault system. We offer comparisons to magnitude and temporal statistical models in section 3. Finally, in section 4, we discuss the broader context and present conclusions.

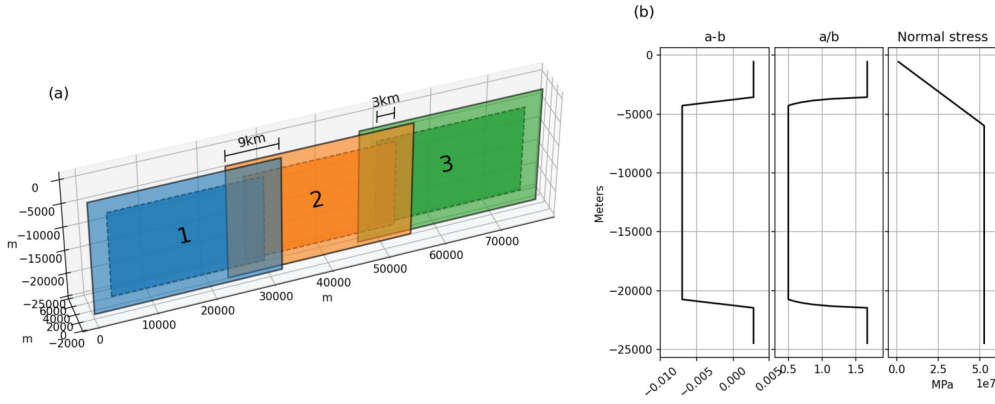


**Fig. 1.** (a) Visualization of the fault model geometry and their numbering. The Opaque patches at each of the fault centers show the velocity-weakening regions. The distribution of frictional parameters is shown in the depth profile in (b). The velocity weakening regions correspond to where  $a - b = -0.007$  and  $a/b = 0.5$ . We set a 1-km transition zone between two frictional regimes. The depth distribution of normal stress linearly increases from 1 MPa at fault top to 52.5 MPa at 6 km and remains constant afterward.

## 2. Method

### 2.1. Problem description

We investigate a system of three *en echelon* right-lateral strike-slip faults inspired by similar fault structures found on multiple observational scales (de Jossineau and Aydin, 2007). We embed these planar faults in a 3-D elastic half-space (Fig. 1a). Each fault has the same geometry and distribution of frictional properties (Fig. 1b). A fault measures 32 km along strike and 24 km along depth, respectively. The faults overlap by 9 km and are 1 km apart. Each fault consists of a seismogenic patch surrounded by 3-km wide velocity-strengthening padding (Fig. 1b). The seismogenic region is then 26 km by 18 km. If we exclude the velocity-strengthening zone, the seismogenic regions overlap by 3 km. We choose the overlap and offset by fixing the fault length, and use scaling relations from field observations for offset and overlap that correspond to our fault length (de Jossineau and Aydin, 2009; Klinger, 2010).

In this study, we focus on the stress interactions between ruptures, including shear stress and normal stress perturbations, and how they impact the earthquake sequences. A strike-slip fault in a half-space does not produce normal stress change on itself, thus isolate the effect of normal stress change to neighboring faults (Oglesby et al., 1998), and assure stress state remain stationary over the entire simulation. Strike-slip faults are also extensively modeled in many preceding studies. Our geometry therefore serves as a starting point and baseline before more variations are added to such simulation.

For reference, we also conduct a simulation with one fault with identical parameters and compare the generated sequences.

### 2.2. Governing equations

The rate-and-state friction law governs the friction evolution on the fault planes. We use the regularized formulation presented by Lapusta et al. (2000); Rice and Ben-Zion (1996), which is valid at near zero slip rates.

$$\mu = a \sinh^{-1} \left[ \frac{V}{2V^*} \exp \left( \frac{\mu^* + b \ln \left( \frac{V^* \theta}{D_{RS}} \right)}{a} \right) \right] \quad (1)$$

Here,  $\mu$  is the friction coefficient;  $V^*$  and  $\mu^*$  are the reference slip rate and the reference friction coefficient; Parameters  $a$  and  $b$  control the contributions of slip rate and fault state to the friction, so that when  $a > b$ , stable sliding will occur, whereas stick-slip

cycles can emerge when  $a < b$  (Fig. 1b).  $D_{RS}$  is the characteristic slip distance over which the state variable  $\theta$  evolves.

We use the Dieterich-Ruina aging law to describe the evolution of the state (Dieterich, 1978; Ruina, 1983):

$$\frac{d\theta}{dt} = 1 - \frac{V\theta}{D_{RS}} \quad (2)$$

The equation of elastostatic equilibrium relates the stress state and friction to the slip rate on a point of a fault (Rice, 1993),

$$\tau_0 + \tau_e - \frac{G}{2c} V = \sigma \mu, \quad (3)$$

where  $\tau_0$  is the background and initial stress;  $\tau_e$  is the elastic shear stress induced by slip on the fault;  $\sigma$  is the combined normal stress from initial condition and fault interaction;  $G$  is the shear modulus and  $c$  is the shear-wave speed.  $G/2c$  is the radiation damping term that approximate inertial effects and bounds the slip rate from unrealistic values.

We use the back-slip approach, such that fault patches exert stress when they slip at a rate different from the plate loading rate  $V_{PL}$  (Savage, 1983; Tullis et al., 2012; Heimissson, 2020). By meshing the fault planes into discrete, non-overlapping dislocations, the shear stress on the left-hand side of (3) of the  $i$ th patch is the sum over all the shear stress imposed by all other patches in the system and can be written as:

$$\tau_i = - \sum_j K_{ij} (\delta_j(t) - V_{PL} t) - \frac{G}{2c} V_i(t), \quad (4)$$

where  $\delta_j$  is the displacement on the  $j$ th patch;  $V_{PL}$  is the loading rate. The stress transfer matrix  $K_{ij}$  contains the stress response of the  $i$ th patch by the unit slip on the  $j$ th patch within the system (van den Ende et al., 2018). The same relation also exists for the normal stress  $\sigma_i$  that also evolve in the simulations. We calculate the matrix  $K_{ij}$  using the rectangular finite dislocation solutions and accompanying module DC3D formulated by Okada (1992).

By taking the time derivative of equation (4) and substituting  $\mu$  with the time derivative of (1), we can obtain two coupled ordinary differential equations (ODEs) of  $\dot{V}$  and  $\dot{\theta}$  from equation (2) for each fault patch (e.g., Rice, 1993; Luo et al., 2017). We perform the simulations using the boundary-element earthquake cycle simulator QDYN (Luo et al., 2017). Galvez et al. (2019) implemented the hierarchical matrix (H-matrix) compression to the stress transfer kernel in QDYN (Bradley, 2014), thus replacing the fast Fourier transform method and allowing non-planar meshes such as a bending, listric or segmented faults.

### 2.3. Relevant parameters

To adequately resolve the nucleation and rupture propagation, the model resolution is tied to two length scales found by the analysis of rate-and-state friction law. Firstly, the cohesive zone or process zone width,  $L_b$ , needs to be three to five times larger than the grid size  $\Delta x$  in boundary integral models (Day et al., 2005), where

$$L_b = \frac{GD_{RS}}{b\sigma}. \quad (5)$$

For 1-D faults, Heimisson (2020) found that the simulation can be resolved with  $L_b/\Delta x$  as low as 1.5, whereas Jiang et al. (2022) take the ratio of 4 for their benchmarks. Following a convergence test (see the supplementary materials), we find that stable nucleation can be achieved with  $L_b/\Delta x$  as low as  $\sim 2.2$ . In this study, we keep the ratio above 3 to assure well resolved cohesive zones and sufficiently accurate simulation, while keeping multi-fault simulations computationally feasible.

The second length scale describes the smallest half-length of an unstable patch, or the nucleation dimension to generate seismic events:  $L_\infty$  (Rubin and Ampuero, 2005), where

$$L_\infty = \frac{GD_c b}{\pi \sigma (b-a)^2}. \quad (6)$$

Seismic events start to appear when seismogenic width  $W$  is larger than  $L_\infty$ . Studies have shown that on a single fault, a complex seismic sequence of full and partial ruptures can emerge when the ratio between  $W$  and  $L_\infty$  is sufficiently large (Barbot, 2019; Cattania, 2019; Heimisson, 2020; Nie and Barbot, 2022). Cattania (2019) found that for a 1-D fault, the minimum ratio to generate two and more events per cycle is  $\sim 10$ . In 2-D plane, the critical nucleation size and rupture regimes depends on the asperity geometry. Cattania and Segall (2019) derive the relevant nucleation size and explore the rupture behavior of circular asperities. The general trend remains the same, that larger ratio between seismogenic patches (or asperity) and critical nucleation size leads to more complex seismicity. We note that in this study the  $W$  is the length of the shorter edge of velocity-weakening patch (Fig. 1) and  $L_\infty$  (equation (6)) taken as the anti-plane value identified by Rubin and Ampuero (2005). Although the scaling is the same, different studies may define these values differently, and we have conformed their values to the definition used here.

In this study, we would like to observe how fault interaction affect seismic sequence. Therefore, we do not create any heterogeneity on the fault planes but expect the fault structure to create complex sequences. By improving the time-stepping efficiency (Appendix A), we can balance large enough  $W/L_\infty$  ratio, well resolved  $L_b$  and reasonable simulation time.

We test the ratios from 10.82 to 32.47 by varying only  $D_{RS}$  and keeping the profiles of  $a$ ,  $b$ , and  $\sigma$  fixed in all simulations. We also test the effect of fault loading rate  $V_{PL}$  on nucleation style using three different values of 5, 35, and 50 mm/year. All other parameters and initial conditions remain the same for all simulations. The exact values are listed in Table 1. An event is registered when an unstable slip's maximum slip rate surpass 0.1 m/second, the speed at which the rupture starts emitting seismic energy (Rubin and Ampuero, 2005).

We initiate all the simulations with the slightly different initial slip rates that equal to 0.99, 1.01, and 1 time  $V_{PL}$  on faults 1, 2, and 3 respectively to offset the event nucleation time on each fault. The initial state is set to  $D_{RS}/V_{PL}$ , which is also the reference state. We run every simulation until there are more than 100 seismic events to have a robust estimation of scaling relationships. The simulations are chaotic right after the first events on

**Table 1**  
Parameter values and model geometries.

Symbol	Description	Value
<b>Material Properties</b>		
$G$	Shear modulus	32 GPa
$\lambda$	Elastic modulus	32 GPa
$c$	Shear wave velocity	3.0 km/s
<b>Frictional Properties</b>		
$\mu^*$	Reference friction coefficient	0.6
$a$	Direct-effect parameter	0.007
$b$	Evolution effect parameter	0.0042–0.016
$D_{RS}$	Critical slip distance	10, 14, 20, 30 mm
$V_{PL}$	Back-slip loading rate	5, 35, 50 mm/year
$V^*$	Reference slip rate	5, 35, 50 mm/year (same as $V_{PL}$ )
$\sigma$	Initial effective normal stress	52.5 MPa
<b>Geometry</b>		
$L_f$	Fault segment length	32 km
$W_f$	Fault segment width	24 km
$L$	Velocity-weakening length	26 km
$W$	Velocity-weakening width	18 km
$O$	Overlapped length	9 km
$S$	Step-over width	1 km
$\Delta x$	grid size	143 m, 200 m

each fault, and therefore we observe no clear spin-up phases (See supplementary figure S1). Each simulation runs on a node of 24 cores and typically takes less than 15 days to finish.

## 3. Result

### 3.1. Earthquake cycles on a single fault

To understand the role of fault system structure and interactions on an earthquake sequence, we explore how a single isolated fault behaves in the relevant parameter range and first perform a simulation with one planar fault as a reference case with of no fault interaction. We set the  $V_{PL}$  at 50 mm/year and the  $W/L_\infty$  ratio as 32.47, the highest we explored with the fault system simulations. Fig. 2a–f present a typical earthquake cycles of a single seismogenic patch. During interseismic times, the creep front penetrates inward, and the locked asperity shrink. Instabilities emerge at the bottom corner and nucleate as a seismic event. The rupture grows and propagates the whole fault. Finally, the afterslip propagates into the creeping zone. Even with the highest  $W/L_\infty$  ratio, the simulation only produces full ruptures and a highly regular sequence for the whole simulated period of 78 earthquake cycles (Fig. 2g). The event magnitudes are capped by the seismogenic patch size at 6.87. The mean recurrence time is 31.14 years, with a coefficient of variation ( $C_v$ ), or the standard deviation over the mean, of 0.02.

### 3.2. Earthquake cycles and sequence statistics of a fault system

We conduct eight simulations of the *en echelon* fault systems in total. For  $D_{RS}$  values of 10 and 14 mm, we simulate three loading rates: 5, 35, and 50 mm/year. We run two simulations using larger  $D_{RS}$  values of 20 mm and 30 mm and a slip rate of 50 mm/year. The full seismic sequences are compiled in supplementary figure S1.

In contrast to the single-fault simulation, a typical seismic cycle from one full rupture on a fault to another consists of several partial ruptures and slow-slip events in between two mainshocks (Fig. 3 and Movie S1). In Fig. 3a, fault 1 on the left has just entered the post-seismic locking stage as the slip rate in a seismogenic patch drops with time (Fig. 3a–d), while faults 2 and 3 are further advanced in their seismic cycles. The slip rate starts to increase at the overlapped area of fault 3, and an event of M5.7 nucleates

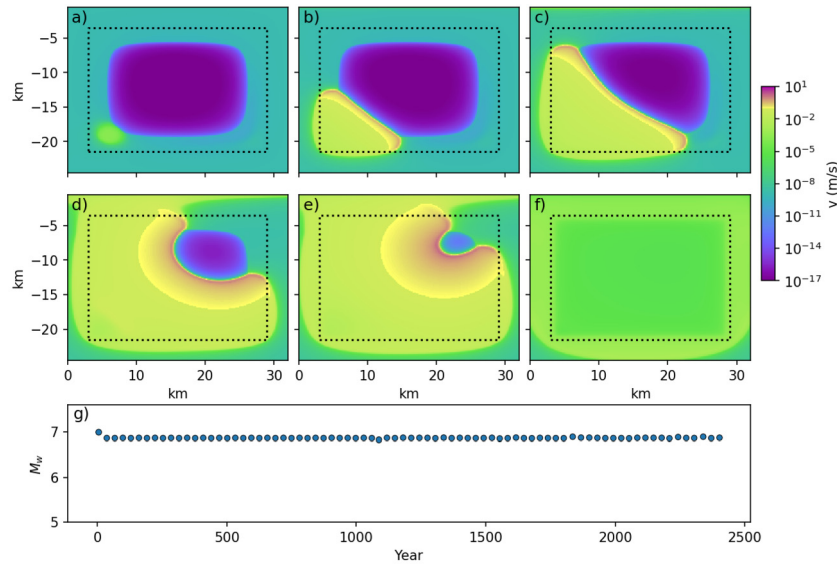


**Fig. 2.** Simulations with a single isolated fault. (a)-(f) Snapshots of a typical earthquake cycle on a single fault and the produced sequence. The slip velocity distinguishes different slipping states. Blueish green represents areas slipping close to the loading rate. Deep purple shows the locked areas under low slip rates. Warm colors indicate areas that are seismically slipping at a slip rate larger than  $10^{-1}$  m/s. Black dashed lines mark the seismogenic zones. (g) The 78 events generated for this simulation has an averaged magnitude of 6.87 except the first event. Without fault system structure, a single fault, in the parameter range explored here, produces only a single periodic event with nearly fixed magnitude.

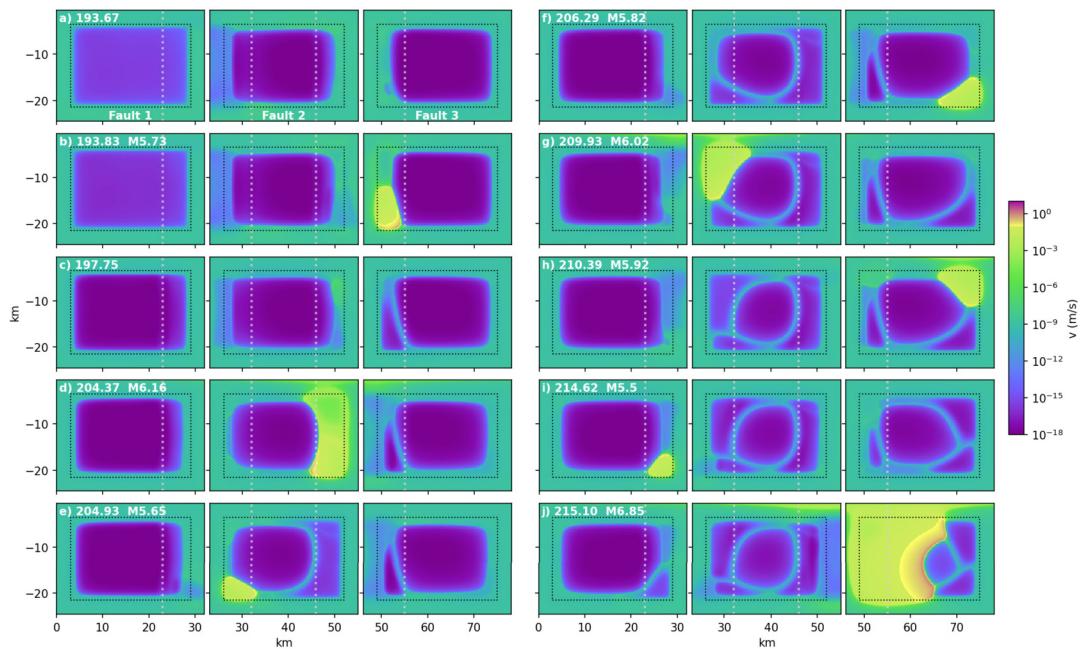


**Fig. 3.** Snapshots of the slip rate field between two full ruptures. Subplots a-j show 10 snapshots in subsequent time (years) and event magnitudes. Warm colors mark the seismically slipping patches with slip rates larger than 0.1 m/sec. Black dashed lines outline the seismogenic velocity-weakening patches. Grey dashed lines mark the overlaps as seen from the side (Fig. 1a). Snapshots are from the simulation with  $W/L_{\infty} = 32.47$  and a loading rate of 50 mm/year. High  $W/L_{\infty}$  ratio lead to many partial ruptures in between full-rupture cycles.

(Fig. 3b). Slow-slip events also occur on the periphery of locked areas (Fig. 3c). Partial ruptures continue to nucleate at the overlapping area and the outer corners, creating patches of “velocity” asperities and irregular seismicity. Finally, a full rupture on fault 3 (Fig. 3j) resets the heterogeneous slip rate distribution and returns the fault state to a homogeneous one, similar to fault 1 in Fig. 3a. In our model, partial ruptures resemble foreshocks before a characteristic event resets the distribution of slip rates and states back to uniform. In addition, partial ruptures cascade around the edge of seismogenic zones while full ruptures propagate the whole seismogenic zone and rupture the foreshock regions again.

We compare the frequency-magnitude distribution and the inter-event time (IET) distribution of the eight simulations. Firstly, our simulations still produce a significant portion of characteristic events and a magnitude gap around M6.5, above which the rupture will be a full one. We find that simulations with a larger  $W/L_{\infty}$  ratio produce partial ruptures with larger  $b$  values on 2-D faults (Fig. 4a), in line with studies performed using 1-D faults (e.g., Catania, 2019; Lambert and Lapusta, 2021). We hypothesize that the  $b$ -value approaches a constant as  $W/L_{\infty}$  becomes larger. A  $W/L_{\infty}$  ratio of 32.47 gives the partial ruptures and  $b$  value of 0.5, while the  $b$  value decreases to 0.3 when the ratio is 23.19. More partial

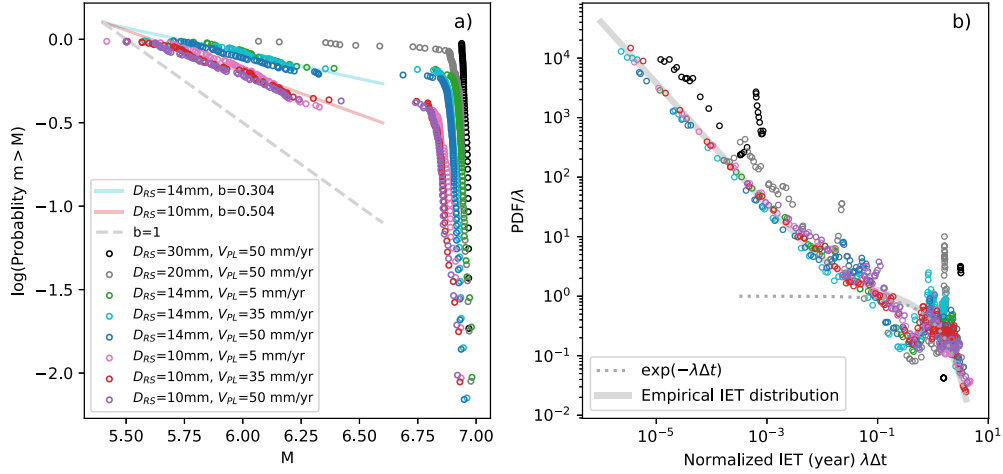


**Fig. 4.** (a) Cumulative frequency-magnitude statistics of events from all eight simulations, showing how likely an event has a magnitude  $m$  larger than magnitude  $M$ . We group catalogs produced with  $D_{RS} = 10\text{mm}$  with warm colors and  $D_{RS} = 14\text{mm}$  with cold colors. Straight lines of corresponding color tones mark the  $b$ -value fit of the partial ruptures. The gray dashed line marks the slope of  $b = 1$ . (b) The probability density functions of inter-event time (IET) of individual catalogs normalized by their seismicity rates  $\lambda$ . The solid gray line shows the empirical inter-event time distribution of Saichev and Sornette (2007). The dashed gray line shows the exponential decay of a Poissonian time series. Both plots show two distinct groups of characteristic events and partial ruptures.

ruptures also mean smaller magnitudes for characteristic events. While the ratio  $W/L_{\infty}$  is important, the loading rates have a minute effect on the partial-rupture  $b$  value in that the  $b$  values seem slightly larger when loading rates are higher, but the effect is negligible compared to the  $W/L_{\infty}$  ratio. We find that for our model setup, partial ruptures cease to emerge at  $W/L_{\infty} = 10.82$  ( $D_c = 30$  mm).

Our catalogs also reproduce the empirical inter-event time distribution and its coefficients proposed by Saichev and Sornette (2007) based on the Omori-Utsu law (Fig. 4b). The relation states that the normalized inter-event time  $\lambda\Delta t$  PDF is

$$f(x) = \left( n\epsilon^{\theta} x^{-1-\theta} + [1 - n + n\epsilon^{\theta} x^{-\theta}]^2 \right) \phi(x, \epsilon), \quad (7)$$

where  $\lambda$  is the seismicity rate, and

$$\phi(x, \epsilon) = \exp\left(- (1-n)x - \frac{n\epsilon^{\theta}}{1-\theta} x^{1-\theta}\right) \quad (8)$$

using the parameters  $n = 0.9$ ,  $\theta = 0.03$ , and  $\epsilon = 0.76$ .

The two simulations with ratios equal to 10.82 and 16.24 deviate from the curve (black and gray circles, respectively), showing that characteristic events plus fault interaction alone do not recreate the empirical inter-event time distribution. These simulations produce synchronized clusters instead (Fig. 5c-d), shown as the bimodal distribution of very short and very long inter-event time.

The remaining six sequences with  $W/L_{\infty}$  ratios of 23.19 and 32.47 fit equation (7) well. A dip can be seen in the simulated inter-event time distribution at the onset of exponential decay around 0.1 normalized time (Fig. 4b), suggesting that our fault system largely produces the two end-member distributions, i.e., the short-term Omori clustering and the long-term Poisson process. The transition between the short-term clustering and independent events is filled either by a more complex fault system or by other physical processes with an intermediate interaction timescale.

### 3.3. Recurrence times

An important aspect of this study is examining the variation of event recurrence under fault interaction. The emergence of an inter-event time distribution similar to the empirically observed ones gives us the confidence to examine the recurrence time statistics and conditional probability of the next event after the occurrence of a full rupture (1) on a fault and 2) within the system.

We compare the four experiment with the same loading rate of 50 mm/year and different  $D_{RS}$  equals 10 mm, 14 mm, 20 mm, 30 mm and observe  $D_{RS}$ 's control on rupture behavior and seismic sequence. For each sequence, we compute the mean recurrence time of full ruptures on individual faults and their  $C_v$  (Fig. 5). The reference single-fault simulation produces a mean recurrence time of 31.15 years under the same loading rate. We find that all cases, except the  $D_{RS} = 10$  mm simulation, produce longer recurrence times than the single-fault simulation. The  $D_{RS} = 10$  mm simulation produces a slightly shorter mean recurrence time of 30.95 years. In all, simulations with more partial ruptures have shorter and more irregular recurrence time (higher  $C_v$ ) than that consists of more full ruptures. The cases with largest  $D_{RS} = 30$  mm produce a synchronized sequence and the longest single-fault recurrence time of 55.56 years.

Variation in recurrence times gives uncertainty to the conditional expectation of the next mainshock on a fault and also the system. We summarize the recurrence times of the six sequences that have good fits to the empirical inter-event time distribution in Fig. 6 by normalizing the times with averaged single-fault recurrence times of each sequence. We calculate the conditional expectation as a cumulative density function (CDF) of the next mainshock occurring on the same fault (pale colors), or in the fault system. For each  $D_{RS}$  we group experiments at different loading rates, given that the inter-event time distribution was not significantly influenced by the loading rate (Fig. 4b). The recurrence time distribution of the single-fault experiment serves as the reference (dark gray line).

The simulations show that, first, the one-fault simulation produces periodic ruptures. Second, the mainshocks on each fault within the system also occur quasi-periodically despite partial ruptures and fault interactions Fig. 6). However, the distribution can spread from 85% to 140% of the mean recurrence time. The distributions resemble a Brownian passage time (BPT) distribution with its mean equal to 1 and aperiodicity equal to the  $C_v$  computed from the simulated sequence (purple dashed line in Fig. 6; Matthews et al., 2002). Finally, from our tests, we do not see  $D_{RS}$  significantly impact the normalized single-fault recurrence time. However, we do see  $D_{RS}$  of 10 mm gives a more varied distribution and a longer tail beyond 140% of the mean recurrence time that is less well-fitted by a BPT distribution. It is not clear if the recurrence time variation is a consequence of our specific model or an intrinsic feature of fault interaction.

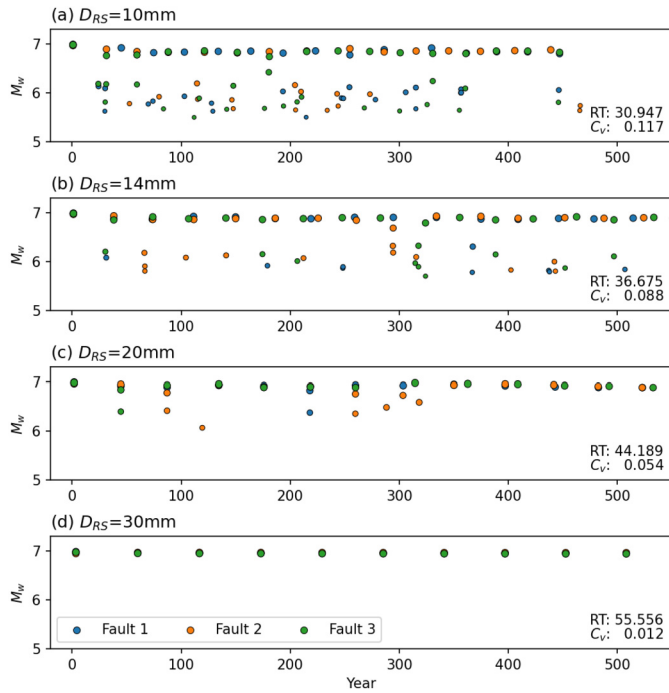


**Fig. 5.** A visualization of event magnitude with time from seismic sequences generated with  $D_{RS}$  ranging from 10 mm in (a) to 30 mm in (d). We show the mean full-rupture recurrence times (RT) and their  $C_v$  at the bottom right. Events on different segments are color-coded following the color scheme in Fig. 1. The figure clearly demonstrates a transition from complex sequences and partial ruptures to synchronized and regular events as  $D_{RS}$  increases.

The system mainshock recurrence time, meaning the time between one mainshock and another mainshock in the system, measures how clustered the system is. If the three faults synchronize like in Fig. 5d, the CDF will form two sharp steps near zero and 1/3. If the mainshocks randomly nucleate, the CDF will be a Poisson process of rate = 3 shown in gray dashed line in Fig. 6. We see the conditional expectation clearly deviates from the null hypothesis of a random series (Fig. 6 red and blue curves). In both cases of  $D_{RS}$  values, a substantial portion of the mainshock pairs occurs within  $\sim 0.04$  normalized recurrence time, representing a significantly heightened chance of another mainshock on neighboring faults. From 0.04 and beyond, the shape of the remaining CDF resembles a wider BPT distribution, with the mean larger than the expected recurrence time (1/3 normalized time). In summary, the sequences are composed of short-term Omori-like clustering and quasi-periodic recurrence, dispersed by interseismic fault interaction. The immediate clustering is noticeably stronger in sequences of  $D_{RS} = 10$  mm comparing to  $D_{RS} = 14$  mm, suggesting that smaller  $D_{RS}$  promote fault clustering. However, beyond the immediate clustering, the remaining recurrence distribution is very similar. The similar distribution is likely due to the stress interaction that is essentially the same in all simulations.

## 4. Discussion

### 4.1. Frequency-magnitude distribution

Our model produces complex sequences that exhibit both characteristic and Gutenberg-Richter-like size distributions and temporal clustering within a simple fault system (Fig. 4, 5). However, comparison to a corresponding single fault system (Fig. 2) reveals that in a minimum system, only characteristic events are produced and no clustering is observed. Thus, we suggest that the emergence of a Gutenberg-Richter type size distribution and event clustering in the three-fault system is a direct consequence of the fault

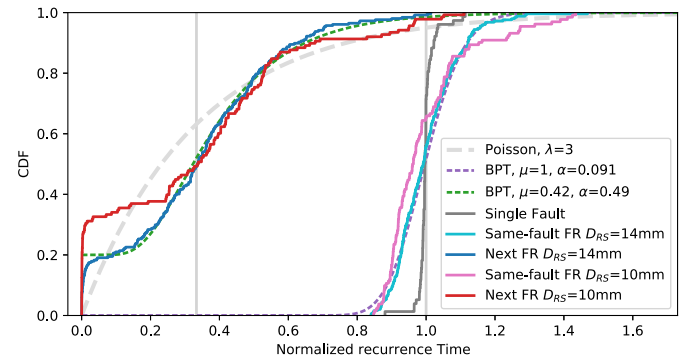


**Fig. 6.** The cumulative density functions (CDF) of full rupture (FR) recurrence times normalized by the averaged single-fault return time. Each curve aggregates the IETs of three simulated catalogs of the same  $D_{RS}$ . Dark gray CDF on the right shows the distribution of single fault recurrence time as the reference. Magenta and cyan CDFs show the single-fault mainshock recurrence time grouped by  $D_{RS} = 10$  mm and 14 mm, respectively. Red and blue CDFs on the left show the system mainshock recurrence times of the same groups. Light gray vertical lines mark the normalized system mean recurrence time 1/3 and same-fault recurrence time 1. The reference CDF of a Poisson process of rate 1/3 is shown as the gray dashed curve. We fit the CDFs of  $D_{RS} = 14$  mm with BPT distributions, plotted in dense dash lines.

system structure and the resulting stress interactions between segments.

The resulting frequency-magnitude distribution of the interacting fault system has two distinct populations (Fig. 4a): a characteristic Gutenberg-Richter type distribution corresponding only to partial ruptures and a narrow distribution of characteristic events corresponding to complete ruptures of a fault. A gap of 0.5 to 0.75 magnitude units separates full and partial ruptures in the frequency magnitude distribution (Fig. 4a). The frequency-magnitude distributions of the partial ruptures show low  $b$  values, which is likely due to the limitation of the ratio of  $W/L_\infty$  that we can reasonably simulate. It is likely that the  $b$ -value would grow larger as the ratio grows, as seen in the 1-D simulations Cattania (2019) conducted.

There are other fault properties like frictional asperities, frictional property distributions or rough surface that induce complex seismicity (Dieterich and Richards-Dinger, 2010; Hillers et al., 2006; Heimisson, 2020). Although these properties also give rise to complex sequences and clustering, few are as observable in seismological and geological observations as geometrical barriers on faults. Segmentation may well be the most important factor that modulate the large earthquakes. Two recent implications of SEAS models hinted the possibility of more insight into the emergence of power-law distribution in large-scale and non-planar fault systems (Uphoff et al., 2022; Ozawa et al., 2022), where we could test the contribution of various factors to the frequency magnitude distribution.

### 4.2. Rupture behaviors in 3-D half-space

We observe that complex seismicity does not occur when we model a single fault plane of  $32 \times 24$  km even with the highest  $W/L_\infty$  value of 35.18 (Movie S2). Partial ruptures on a single fault emerges when the nucleated events are small enough to arrest before penetrating the locked asperity. The exact ratio depends on the length scale  $L_\infty$ , that also depends on the asperity geometry. Barbot (2021) generated partial ruptures with a low  $W/L_\infty$  of 5.33 with an elongated fault measured 75 km by 10 km. Cattania and Segall (2019) found the ratio to be an equivalent of  $W/L_\infty = 29.6$  for a circular asperity. Our velocity-weakening patch has a length to width ratio of 1.44 and therefore could require higher  $W/L_\infty$  to create self-arrest earthquakes.



Another possible factor influencing the rupture behaviors besides asperity geometry is the loading method. Here, we load the fault using the back-slip approach (equation (4)), where the stress transfer is determined by the slip rate difference between the patch and the loading rate. This approach creates a smoother stressing field than faults loaded by adjacent creeping regions (e.g., Cattania and Segall, 2019). The sharp stressing rate contrast enforced by creeping promote nucleation on the creeping edge and arrests when reaching the low-stress region, therefore creating partial ruptures at smaller  $W/L_\infty$ . In our simulation, the stress interaction by multiple faults creates a heterogeneous stress field and promotes partial ruptures in our system. All events, except the initial one, nucleate exclusively on the corners and step-overs once the stress field evolves away from the initial homogeneous stress and velocity field (Fig. 3; Movie S1). Stress heterogeneity also sometimes restrict the partial events within the overlapped area (Fig. 3d).

We do not observe multi-segment events in our simulations, meaning no rupture jumps from one segment to another while the peak slip rate stays above  $10^{-1}$  m/s. The shortest inter-event time we observe is four minutes between a foreshock-mainshock pair on the same fault. Multi-fault ruptures have been observed in many recent major earthquakes (Ross et al., 2019; Hamling et al., 2017) and are the subject of many studies in estimating their possible hazard impact (Page et al., 2014; Chartier et al., 2017). They impact a current study to increase the maximum jumping distance from 5 km to 15 km (Page et al., 2014; Milner et al., 2022). Lambert and Lapusta (2021) performed rupture jumping experiments on two adjacent faults using both fully dynamic and quasi-dynamic simulations. They confirmed that a rupture can jump between segments via dynamic stress transfer, whereas no rupture jumps for the quasi-dynamic case. However, the jump rate is highly sensitive to the model parameters. Whether the rupture continues after the jump may also depend on where the current state favor continued rupture. In addition, current SEAS models are yet to consider heterogeneous bulk properties. Thus, more development is needed to adequately address multi-fault rupture likelihood and its impact on the seismicity statistics in the presence of dynamic triggering.

In all cases, we see stress perturbation's importance in modulating the seismic sequence. And how simulation implements such realistic perturbation impact the simulation outcome. Loading the fault with steady creep is perhaps a more physical way compared to the back-slip approach. However, back-slipping ensure the stress does not diverge over many seismic cycles and provide a simple way to stress multiple, geometrically complicated faults. With the improved efficiency of SEAS models, further development should focus on advancing the stress interaction methods or shift to volumetric numerical methods for ruptures over many seismic cycles.

#### 4.3. Earthquake recurrence and implication for seismic hazard

Our result indicates that the segmented geometry plays a role in producing the power-law distributed seismicity. In addition, the emergence of partial ruptures creates stress heterogeneity and velocity heterogeneity to desynchronize mainshock occurrence (e.g., Fig. 5c-d) and change the mean recurrence time. Using our setup, we can easily compute conditional expectation of the next large earthquake within our system (section 3.3). Our statistics are similar to what Barbot (2021) observed in a system of four parallel faults, where the mainshocks appears more synchronized when  $W/L_\infty$  is higher. We can see the sequences are controlled by short-term clustering and a weaker interseismic fault interaction. Within the fault system, one can expect a chance as high as 30% that the next mainshock follows soon after. Experiments of higher  $W/L_\infty$  have higher proportion of clustered mainshocks. From our results, each individual fault's recurrence time largely falls within

20% around the mean, and we observe a heightened chance of another full ruptures on other faults Fig. 6b.

The simple geometrical barriers that exist in crustal strike-slip faults also exist in the dipping direction in megathrusts like the Main Himalayan Thrust. The steep ramp concentrates partial ruptures in between through-going events that reach the surface and modulate the large earthquake cycle (Dal Zilio et al., 2019; Sathikumar and Barbot, 2021). We also see a plausible analog to our fault system in the central Apennines fault system. It is known to produce clustered sequences (Wedmore et al., 2017). The fault system is composed of segmented and overlapping normal faults of similar lengths and slip rates, and slick carbonate faults (e.g., Han et al., 2007) that can promote synchronization. It is likely that the fault interaction between similar faults promote a heightened chance of mainshock clustering.

There remain several relevant geometrical parameters that may affect the modeled recurrence statistics, e.g., different segment loading rates, other complex geometries, different faulting types, heterogeneous friction properties, and more. For example, when building a fault database for hazard models, the long-term slip rates often have the largest uncertainty (e.g., Basili et al., 2013). Simple block models that mimic asperities of different strength on the same subduction zone form chaotic interactions (Huang and Turcotte, 1990). Experiments with the loading rate sensitivity will show how the conditional expectation of the next event changes from a single fault to faults within a system. Moreover, we could verify the uncertainties of current seismic hazard models by systematically exploring different parameters with earthquake cycle modeling with a more efficient model we propose.

Finally, we look at the long-standing debate in seismology on whether faults and fault systems show Gutenberg-Richter or characteristic earthquake distributions in size and in return time (Jackson, 2006). Our results suggest that not only individual faults but also fault systems can exhibit characteristic Gutenberg-Richter behavior. In our simulations, we see that events of many magnitudes can occur, with a power-law size distribution, but only up to the threshold of  $\sim M6.3$  confined by the area of stress interaction (Fig. 4a). Beyond the threshold, all ruptures will be run-away full ruptures of magnitude 6.5 to 6.9. In addition, the mainshock remain quasi-periodic. This behavior of dual Gutenberg-Richter and characteristic event behavior is, for example, observed in the paleoseismic events of the Alpine Fault of New Zealand (Berryman et al., 2012). Our identical, homogeneous faults seem to mimic a mature and isolated fault like the Alpine Fault, with geometrical gaps that modulate the rupture extent (Howarth et al., 2021). A more continuous magnitude-frequency distribution likely instead emerges from complex geometries and fault heterogeneity.

## 5. Conclusion

We perform earthquake cycle simulations using a 3-D strike-slip fault system. By improving solver efficiency, we accumulate enough seismic events that reveal the frequency-magnitude relations and temporal clustering. Furthermore, we can extract fault-based recurrence-time statistics that is an important reference for fault-based hazard assessment.

Our result shows that a simple simulated fault system, which resembles natural fault geometry, can generate realistic earthquake statistics, including a Gutenberg-Richter size distribution, a simultaneous characteristic event distribution, and an inter-event time distribution that is highly correlated with the empirical law. The simulations provide insight into the occurrence of the Gutenberg-Richter size distribution, which represent partial ruptures that occur from fault interaction. The distribution of characteristic events represents only full fault ruptures. Without fault interactions, no partial ruptures occur and the frequency magnitude distribution

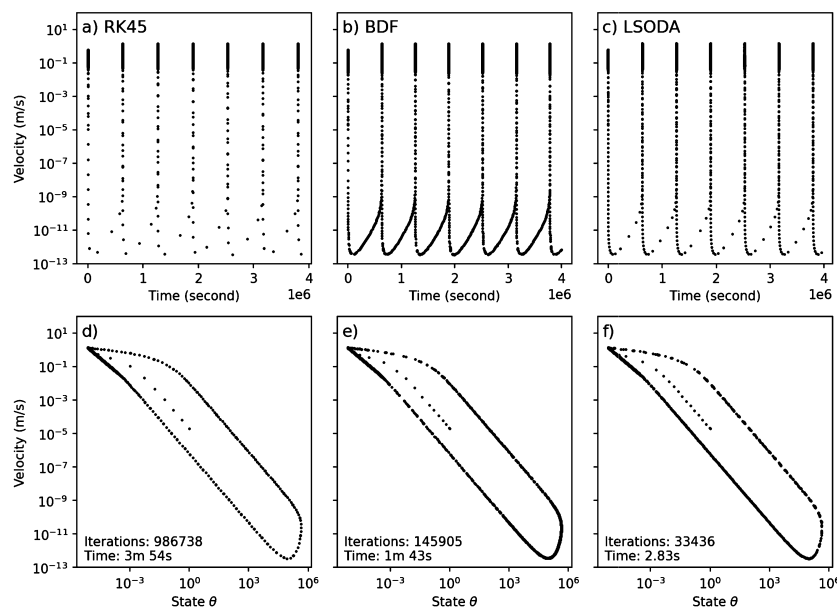


**Fig. 7.** Performance comparison of the RK45, BDF and LSODA solver (left, center, and right column respectively) using a spring-block 1-D fault. The upper row (a-c) shows the block velocity with time, showing five events over a time span of  $5 \times 10^6$  seconds. We plot one dot every 10 iterations to reduce clutter. The lower row (d-f) shows the limit cycles formed by the velocity and the state variable  $\theta$ .

represents only characteristic events. These statistics are not prescribed in the model, but emerge from first-order physical representation and interaction between faults. Emergence of partial ruptures promotes varied recurrence times and increases the probability of clustering of mainshocks. We show that larger  $W/L_\infty$  leads to higher probability of mainshock clustering and larger recurrence time variation. Because our models are well resolved in the continuum domain, it preserves rich and realistic slip behaviors independent of model meshing.

The modeling approach we present here could readily be adapted to more complex fault systems and consider observed fault geometries and slip rates. The advances in computational efficiency that we include offers first steps towards simulation-based, time-dependent rupture forecasts with 3-D continuum models. A plausible use case can be forecasting subduction-zone events by assimilating past ruptures on a realistic geometry.

#### CRediT authorship contribution statement

**Yifan Yin:** Conceptualization, Formal analysis, Investigation, Methodology, Software, Visualization, Writing – original draft. **Percy Galvez:** Conceptualization, Methodology, Software, Writing – review & editing. **Elías Rafn Heimissson:** Funding acquisition, Investigation, Validation, Writing – review & editing. **Stefan Wiemer:** Conceptualization, Funding acquisition, Resources, Supervision, Writing – review & editing.

#### Declaration of competing interest

The authors declare that they have no known competing financial interests or personal relationships that could have appeared to influence the work reported in this paper.

#### Data availability

No data was used for the research described in the article.

#### Acknowledgements

The authors have no conflicts of interest to declare. This research is funded by SED credit number 22818. ERH acknowledges

funding from the ETH Zürich Postdoctoral Fellowship (Project No. FEL-19 20-2). YY would like to thank Dr. P. A. Selvadurai and Dr. A. P. Rinaldi for the valuable discussions. The authors thank editor Prof. Rebecca Bendick, reviewer prof. B. A. Erickson, and two anonymous reviewers, who's critical comments substantially improved the manuscript. The simulations are carried out on the ETH Zürich Euler cluster.

#### Appendix A. Numerical method

In this study, we further improve QDYN's time-stepping efficiency by implementing the LSODA solver (Hindmarsh, 1983; Petzold, 1983). We demonstrate the bottleneck in solving earthquake cycle by solving a 1-D spring-block model using three ODE solvers: the explicit Runge-Kutta solver (RK45), the implicit BDF solver and the hybrid LSODA solver on a laptop. The 1-D fault is governed by the classical rate-and-state friction and aging law for the state evolution.

Fig. 7 demonstrate how different solvers adapt to the rate-and-state evolution. The system of ODEs becomes stiff when velocity start to decay after the seismic pulses. The stiff periods manifest as concentrated iterations shown in the velocity peaks in Fig. 7a-c, and the upper-right corner of the limit cycles in Fig. 7d-f. Explicit solvers like the Runge-Kutta methods require small time-steps to be numerically stable (Erickson et al., 2008) and spend the majority of calculation in this period. This becomes a problem when we attempt to simulate multiple seismic events in a reasonable time. BDF performs better in terms of time steps, but it also requires smaller time steps through the interseismic times. The LSODA solver monitors the stiffness of the system and automatically switches between Adams methods (predictor-corrector) in the non-stiff case and backward differentiation formula (BDF) methods (Gear methods) in the stiff case. The algorithm vastly reduced calculation time and more evenly solved model evolutions.

When using a Runge-Kutta solver for three 3 planar faults, a full rupture takes approximately 9,000 time-steps, while interseismic periods take around 500,000 time-steps. After switching solver, a full rupture on a fault section takes about 22,000 time-steps, while an extended interseismic period takes around 37,000 time-steps to complete.

## Appendix B. Supplementary material

Supplementary material related to this article can be found online at <https://doi.org/10.1016/j.epsl.2023.118056>.

## References

- Bak, P., Tang, C., 1989. Earthquakes as a self-organized critical phenomenon. *J. Geophys. Res.* 94, 635–637. <https://doi.org/10.1029/JB094iB11p15635>.
- Barbot, S., 2019. Slow-slip, slow earthquakes, period-two cycles, full and partial ruptures, and deterministic chaos in a single asperity fault. *Tectonophysics* 768, 228171. <https://doi.org/10.1016/j.tecto.2019.228171>.
- Barbot, S., 2021. A spectral boundary-integral method for quasi-dynamic ruptures of multiple parallel faults. *Bull. Seismol. Soc. Am.* 111, 1614–1630. <https://doi.org/10.1785/0120210004>.
- Basili, R., Kastelic, V., Demircioglu, M.B., Garcia Moreno, D., Nemser, E.S., Petricca, P., Sboras, S.P., Besana-Ostman, G.M., Cabral, J., Camelbeeck, T., Caputo, R., Danciu, L., Domaç, H., Fonseca, J.F.d.B.D., García-Mayordomo, J., Giardini, D., Glavatic, B., Gulen, L., Ince, Y., Pavlides, S., Sesetyan, K., Tarabusi, G., Tiberti, M.M., Utkucu, M., Valensise, G., Vanneste, K., Vilanova, S.P., Wössner, J., 2013. European database of seismogenic faults (EDSF). <https://doi.org/10.6092/INGV.IT-SHARE-EDSF>.
- Ben-Zion, Y., 2008. Collective behavior of earthquakes and faults: continuum-discrete transitions, progressive evolutionary changes, and different dynamic regimes. *Rev. Geophys.* 46, RG4006. <https://doi.org/10.1029/2008RG000260>.
- Berryman, K.R., Cochran, U.A., Clark, K.J., Biasi, G.P., Langridge, R.M., Villamor, P., 2012. Major earthquakes occur regularly on an isolated plate boundary fault. *Science* 336, 1690–1693. <https://doi.org/10.1126/science.1218959>.
- Bradley, A.M., 2014. Software for efficient static dislocation-traction calculations in fault simulators. *Seismol. Res. Lett.* 85, 1358–1365. <https://doi.org/10.1785/0220140092>.
- Cattania, C., 2019. Complex earthquake sequences on simple faults. *Geophys. Res. Lett.* 46, 10384–10393. <https://doi.org/10.1029/2019GL083628>.
- Cattania, C., Segall, P., 2019. Crack models of repeating earthquakes predict observed moment-recurrence scaling. *J. Geophys. Res., Solid Earth* 124, 476–503. <https://doi.org/10.1029/2018jb016056>.
- Chartier, T., Scotti, O., Lyon-Caen, H., Boiselet, A., 2017. Methodology for earthquake rupture rate estimates of fault networks: example for the western Corinth rift, Greece. *Nat. Hazards Earth Syst. Sci.* 17, 1857–1869. <https://doi.org/10.5194/nhess-17-1857-2017>.
- Colella, H.V., Dieterich, J.H., Richards-Dinger, K.B., 2011. Multi-event simulations of slow slip events for a Cascadia-like subduction zone. *Geophys. Res. Lett.* 38. <https://doi.org/10.1029/2011GL048817>.
- Dal Zilio, L., van Dinther, Y., Gerya, T.V., Avouac, J.P., 2019. Bimodal seismicity in the Himalaya controlled by fault friction and geometry. *Nat. Commun.* 10, 1–11. <https://doi.org/10.1038/s41467-018-07874-8>.
- Day, S.M., Dalguer, L.A., Lapusta, N., Liu, Y., 2005. Comparison of finite difference and boundary integral solutions to three-dimensional spontaneous rupture. *J. Geophys. Res.* 110. <https://doi.org/10.1029/2005jb003813>.
- Dieterich, J.H., 1978. Time-dependent friction and the mechanics of stick-slip. *Pure Appl. Geophys.* 116, 790.
- Dieterich, J.H., Richards-Dinger, K.B., 2010. Earthquake recurrence in simulated fault systems. *Pure Appl. Geophys.* 167, 1087–1104. <https://doi.org/10.1007/s00024-010-0094-0>.
- Dublanchet, P., 2020. Stress-dependent b value variations in a heterogeneous rate-and-state fault model. *Geophys. Res. Lett.* 47. <https://doi.org/10.1029/2020gl087434>.
- van den Ende, M.P.A., Chen, J., Ampuero, J.P., Niemeijer, A.R., 2018. A comparison between rate-and-state friction and microphysical models, based on numerical simulations of fault slip. *Tectonophysics* 733, 273–295. <https://doi.org/10.1016/j.tecto.2017.11.040>.
- Erickson, B.A., Birnir, B., Lavallée, D., 2008. A model for aperiodicity in earthquakes. *Nonlinear Process. Geophys.* 15, 1–12. <https://doi.org/10.5194/npg-15-1-2008>.
- Erickson, B.A., Jiang, J., Barall, M., Lapusta, N., Dunham, E.M., Harris, R., Abrahams, L.S., Allison, K.L., Ampuero, J., Barbot, S., Cattania, C., Elbanna, A., Fialko, Y., Idini, B., Kozdon, J.E., Lambert, V., Liu, Y., Luo, Y., Ma, X., McKay, M.B., Segall, P., Shi, P., van den Ende, M., Wei, M., 2020. The community code verification exercise for simulating sequences of earthquakes and aseismic slip (SEAS). *Seismol. Res. Lett.* 91, 874–890. <https://doi.org/10.1785/0220190248>.
- Field, E.H., 2019. How physics-based earthquake simulators might help improve earthquake forecasts. *Seismol. Res. Lett.* 90, 467–472. <https://doi.org/10.1785/0220180299>.
- Field, E.H., Milner, K.R., Hardebeck, J.L., Page, M.T., van der Elst, N.J., Jordan, T.H., Michael, A.J., Shaw, B.E., Werner, M.J., 2017. A spatiotemporal clustering model for the third uniform California earthquake rupture forecast (UCERF3-ETAS): toward an operational earthquake forecast. *Bull. Seismol. Soc. Am.* 107. <https://doi.org/10.1785/0120160173>.
- Galvez, P., Somerville, P., Petukhin, A., Ampuero, J.P., Peter, D., 2019. Earthquake cycle modelling of multi-segmented faults: dynamic rupture and ground motion simulation of the 1992 MW 7.3 landers earthquake. *Pure Appl. Geophys.* <https://doi.org/10.1007/s00024-019-02228-x>.
- Gutenberg, B., Richter, C.F., 1944. Frequency of earthquakes in California. *Bull. Seismol. Soc. Am.* 34, 185–188. <https://doi.org/10.1785/BSSA0340040185>.
- Hamling, I.J., Hreinsdóttir, S., Clark, K.J., Elliott, J., Liang, C., Fielding, E.J., Litchfield, N.J., Villamor, P., Wallace, L.M., Wright, T.J., D'Anastasio, E., Bannister, S.C., Burbidge, D., Denys, P., Gentile, P., Howarth, J., Mueller, C., Palmer, N., Pearson, C., Power, W., Barnes, P.M., Barrell, D.J.A., Van Dissen, R., Langridge, R., Little, T.A., Nicol, A., Pettinga, J.R., Rowland, J., Stirling, M.W., 2017. Complex multifault rupture during the 2016 M w 7.8 kaikōura earthquake, New Zealand. *Science* 356, eaam7194. <https://doi.org/10.1126/science.aam7194>.
- Han, R., Shimamoto, T., Hirose, T., Ree, J.H., Ando, J.I., 2007. Ultralow friction of carbonate faults caused by thermal decomposition. *Science* 316, 878–881. <https://doi.org/10.1126/science.1139763>.
- Heimonsson, E.R., 2020. Crack to pulse transition and magnitude statistics during earthquake cycles on a self-similar rough fault. *Earth Planet. Sci. Lett.* 537, 116202. <https://doi.org/10.1016/j.epsl.2020.116202>.
- Hillers, G., Ben-zion, Y., Mai, P.M., 2006. Seismicity on a fault controlled by rate- and state-dependent friction with spatial variations of the critical slip distance. *J. Geophys. Res.* 111, B01403. <https://doi.org/10.1029/2005jb003859>.
- Hillers, G., Mai, P.M., Ben-Zion, Y., Ampuero, J.P., 2007. Statistical properties of seismicity of fault zones at different evolutionary stages. *Geophys. J. Int.* 169, 515–533. <https://doi.org/10.1111/j.1365-246X.2006.03275.x>.
- Hindmarsh, A.C., 1983. ODEPACK, a systematized collection of ODE solvers. *IMACS Trans. Sci. Comput.* 1, 55–64.
- Howarth, J.D., Barth, N.C., Fitzsimons, S.J., Richards-Dinger, K., Clark, K.J., Biasi, G.P., Cochran, U.A., Langridge, R.M., Berryman, K.R., Sutherland, R., 2021. Spatiotemporal clustering of great earthquakes on a transform fault controlled by geometry. *Nat. Geosci.* <https://doi.org/10.1038/s41561-021-00721-4>.
- Huang, J., Turcotte, D.L., 1990. Evidence for chaotic fault interactions in the seismicity of the San Andreas fault and Nankai trough. *Nature* 348, 234–236. <https://doi.org/10.1038/348234a0>.
- Jackson, J., 2006. Fatal attraction: living with earthquakes, the growth of villages into megacities, and earthquake vulnerability in the modern world. *Philos. Trans. A Math. Phys. Eng. Sci.* 364, 1911–1925. <https://doi.org/10.1098/rsta.2006.1805>.
- Jiang, J., Erickson, B.A., Lambert, V.R., Ampuero, J.P., Ando, R., Barbot, S.D., Cattania, C., Zilio, L.D., Duan, B., Dunham, E.M., Gabriel, A.A., Lapusta, N., Li, D., Li, M., Liu, D., Liu, Y., Ozawa, S., Pranger, C., van Dinther, Y., 2022. Community-driven code comparisons for three-dimensional dynamic modeling of sequences of earthquakes and aseismic slip. *J. Geophys. Res., Solid Earth* 127. <https://doi.org/10.1029/2021jb023519>.
- Jiménez, A., 2013. Cellular automata to describe seismicity: a review. *Acta Geophys.* 61, 1325–1350. <https://doi.org/10.2478/s11600-013-0144-y>.
- de Jossineau, G., Aydin, A., 2007. The evolution of the damage zone with fault growth in sandstone and its multiscale characteristics. *J. Geophys. Res.* 112. <https://doi.org/10.1029/2006jb004711>.
- de Jossineau, G., Aydin, A., 2009. Segmentation along strike-slip faults revisited. *Pure Appl. Geophys.* 166, 1575–1594. <https://doi.org/10.1007/s00024-009-0511-4>.
- Klinger, Y., 2010. Relation between continental strike-slip earthquake segmentation and thickness of the crust. *J. Geophys. Res.* 115, B07306. <https://doi.org/10.1029/2009JB006550>.
- Lambert, V., Lapusta, N., 2021. Resolving simulated sequences of earthquakes and fault interactions: implications for physics-based seismic hazard assessment. *J. Geophys. Res., Solid Earth* 126. <https://doi.org/10.1029/2021jb022193>.
- Lapusta, N., Rice, J.R., Ben-Zion, Y., Zheng, G., 2000. Elastodynamic analysis for slow tectonic loading with spontaneous rupture episodes on faults with rate- and state-dependent friction. *J. Geophys. Res.* 105, 23765–23789. <https://doi.org/10.1029/2000jb900250>.
- Luo, Y., Ampuero, J.P., Galvez, P., van den Ende, M.P.A., Idini, B., 2017. QDYN: a Quasi-DYNAMIC earthquake simulator (v1.1).
- Matthews, M.V., Ellsworth, W.L., Reasenber, P.A., 2002. A Brownian model for recurrent earthquakes. *Bull. Seismol. Soc. Am.* 92, 2233–2250. <https://doi.org/10.1785/0120010267>.
- Milner, K.R., Shaw, B.E., Field, E.H., 2022. Enumerating plausible multifault ruptures in complex fault systems with physical constraints. *Bull. Seismol. Soc. Am.* 112, 1806–1824. <https://doi.org/10.1785/0120210322>.
- Milner, K.R., Shaw, B.E., Goulet, C.A., Richards-Dinger, K.B., Callaghan, S., Jordan, T.H., Dieterich, J.H., Field, E.H., 2021. Toward physics-based nonergodic PSHA: a prototype fully deterministic seismic hazard model for southern California. *Bull. Seismol. Soc. Am.* 111, 898–915. <https://doi.org/10.1785/0120200216>.
- Nie, S., Barbot, S., 2022. Rupture styles linked to recurrence patterns in seismic cycles with a compliant fault zone. *Earth Planet. Sci. Lett.* 591, 117593. <https://doi.org/10.1016/j.epsl.2022.117593>.
- Ogata, Y., 1988. Statistical models for earthquake occurrences and residual analysis for point processes. *J. Am. Stat. Assoc.* 83, 9–27. <https://doi.org/10.1080/01621459.1988.10478560>.
- Oglesby, D.D., Archuleta, R.J., Nielsen, S.B., 1998. Earthquakes on dipping faults: the effects of broken symmetry. *Science* 280, 1055–1059. <https://doi.org/10.1126/science.280.5366.1055>.

- Okada, Y., 1992. Internal deformation due to shear and tensile faults in a half-space. *Bull. Seismol. Soc. Am.* 82, 1018–1040. <https://doi.org/10.1785/BSSA0820021018>.
- Omori, F., 1895. On the aftershocks of earthquakes. *J. Coll. Sci.* 7, 111–120.
- Ozawa, S., Ida, A., Hoshino, T., Ando, R., 2022. Large-scale earthquake sequence simulations on 3D nonplanar faults using the boundary element method accelerated by lattice h-matrices. *Geophys. J. Int.* 232. <https://doi.org/10.1093/gji/ggac386>.
- Page, M.T., Field, E.H., Milner, K.R., Powers, P.M., 2014. The UCERF3 grand inversion: solving for the long-term rate of ruptures in a fault system. *Bull. Seismol. Soc. Am.* 104, 1181–1204. <https://doi.org/10.1785/0120130180>.
- Petzold, L., 1983. Automatic selection of methods for solving stiff and nonstiff systems of ordinary differential equations. *SIAM J. Sci. Stat. Comput.* 4, 136–148. <https://doi.org/10.1137/0904010>.
- Rice, J.R., 1993. Spatio-temporal complexity of slip on a fault. *J. Geophys. Res.* 98, 9885. <https://doi.org/10.1029/93jb00191>.
- Rice, J.R., Ben-Zion, Y., 1996. Slip complexity in earthquake fault models. *Proc. Natl. Acad. Sci. USA* 93, 3811–3818. <https://doi.org/10.1073/pnas.93.9.3811>.
- Richards-Dinger, K.B., Dieterich, J.H., 2012. RSQSim earthquake simulator. *Seismol. Res. Lett.* 83, 983–990. <https://doi.org/10.1785/0220120105>.
- Robinson, R., Benites, R., 1995. Synthetic seismicity models of multiple interacting faults. *J. Geophys. Res.* 100, 18229. <https://doi.org/10.1029/95jb01569>.
- Ross, Z.E., Idini, B., Jia, Z., Stephenson, O.L., Zhong, M., Wang, X., Zhan, Z., Simons, M., Fielding, E.J., Yun, S.H., Hauksson, E., Moore, A.W., Liu, Z., Jung, J., 2019. Hierarchical interlocked orthogonal faulting in the 2019 ridgecrest earthquake sequence. *Science* 366, 346–351. <https://doi.org/10.1126/science.aaz0109>.
- Rubin, A.M., Ampuero, J.P., 2005. Earthquake nucleation on (aging) rate and state faults. *J. Geophys. Res.* 110, 1–24. <https://doi.org/10.1029/2005jb003686>.
- Ruina, A., 1983. Slip instability and state variable friction laws. *J. Geophys. Res., Solid Earth* 88, 10359–10370. <https://doi.org/10.1029/JB088iB12p10359>.
- Rundle, J.B., 1988. A physical model for earthquakes: 1. Fluctuations and interactions. *J. Geophys. Res., Solid Earth* 93, 6237–6254. <https://doi.org/10.1029/JB093iB06p06237>.
- Saichev, A., Sornette, D., 2007. Theory of earthquake recurrence times. *J. Geophys. Res.* 112. <https://doi.org/10.1029/2006jb004536>.
- Sathiakumar, S., Barbot, S., 2021. The stop-start control of seismicity by fault bends along the main Himalayan thrust. *Commun. Earth Environ.* 2, 1–11. <https://doi.org/10.1038/s43247-021-00153-3>.
- Savage, J.C., 1983. A dislocation model of strain accumulation and release at a subduction zone. *J. Geophys. Res.* 88, 4984–4996. <https://doi.org/10.1029/jb088ib06p04984>.
- Schorlemmer, D., Werner, M.J., Marzocchi, W., Jordan, T.H., Ogata, Y., Jackson, D.D., Mak, S., Rhoades, D.A., Gerstenberger, M.C., Hirata, N., Liukis, M., Maechling, P.J., Strader, A., Taroni, M., Wiemer, S., Zechar, J.D., Zhuang, J., 2018. The laboratory for the study of earthquake predictability: achievements and priorities. *Seismol. Res. Lett.* 89, 1305–1313. <https://doi.org/10.1785/0220180053>.
- Shaw, B.E., Milner, K.R., Field, E.H., Richards-Dinger, K., Gilchrist, J.J., Dieterich, J.H., Jordan, T.H., 2018. A physics-based earthquake simulator replicates seismic hazard statistics across California. *Sci. Adv.* 4, eaau0688. <https://doi.org/10.1126/sciadv.aau0688>.
- Taroni, M., Marzocchi, W., Schorlemmer, D., Werner, M.J., Wiemer, S., Zechar, J.D., Heiniger, L., Euchner, F., 2018. Prospective CSEP evaluation of 1-day, 3-month, and 5-yr earthquake forecasts for Italy. *Seismol. Res. Lett.* 89, 1251–1261. <https://doi.org/10.1785/0220180031>.
- Tse, S.T., Rice, J.R., 1986. Crustal earthquake instability in relation to the depth variation of frictional slip properties. *J. Geophys. Res.* 91, 9452. <https://doi.org/10.1029/jb091ib09p09452>.
- Tullis, T.E., Richards-Dinger, K.B., Barall, M., Dieterich, J.H., Field, E.H., Heien, E.M., Kellogg, L.H., Pollitz, F.F., Rundle, J.B., Sachs, M.K., Turcotte, D.L., Ward, S.N., Yikilmaz, M.B., 2012. Generic earthquake simulator. *Seismol. Res. Lett.* 83, 959–963. <https://doi.org/10.1785/0220120093>.
- Uphoff, C., May, D.A., Gabriel, A.A., 2022. A discontinuous Galerkin method for sequences of earthquakes and aseismic slip on multiple faults using unstructured curvilinear grids. *Geophys. J. Int.* <https://doi.org/10.1093/gji/ggac467>.
- Utsu, T., 1961. A statistical study on the occurrence of aftershocks. *Geophys. Mag.* 30, 521–605.
- Wedmore, L.N.J., Faure Walker, J.P., Roberts, G.P., Sammonds, P.R., McCaffrey, K.J.W., Cowie, P.A., 2017. A 667 year record of coseismic and interseismic Coulomb stress changes in central Italy reveals the role of fault interaction in controlling irregular earthquake recurrence intervals. *J. Geophys. Res., Solid Earth* 122, 5691–5711. <https://doi.org/10.1002/2017jb014054>.